Mechanical behavior of BNNT/PM/CF composite shells in flexure using finite element method and first-order shear deformation theory

Mehdi billah ouassim*[1], Mustapha Fouaidi[1,2], Laidi Zahiri[1], Naoual Belouaggadiaa[1],Yassine EL Kiri[1]

[1]Laboratory of Modelling and Simulation of Intelligent Industrial Systems (M2S2I) ENSET, Hassan II University of Casablanca, Morocco
[2]Mechanical and Energy (ME) group, LPNAMME laboratory, Department of Physics, Faculty of Sciences, Chouaib Doukkali University, P.B 20, 24000 El Jadida, Morocco

Abstract. This study investigates the flexural behavior of composite cylindrical panels (CCPs) subjected to static loads (SLs) under various boundary conditions (BCs). The CCPs consist of a polymer matrix (PM) reinforced by a combination of two reinforcements at different scales: single-walled boron nitride nanotubes (SWBNNTs) with a functionally graded (FG) distribution and uniformly distributed carbon fibers (CFs). The material properties of the CCPs are evaluated using a hybrid homogenization procedure (HHP) combining the Halpin–Tsai (HT) model, the rule of mixtures (RM), and a micromechanical approach (MMA). The governing equations (GEs) for flexural behavior are derived from the first-order shear deformation theory (FSDT), while the finite element method (FEM) is employed to determine the panel deformations. The validity of the proposed approach is demonstrated, followed by illustrative parametric studies aimed at examining the effect of different reinforcement schemes on the flexural response of the cylindrical nanocomposite panels, as well as the influence of the SWBNNT and CF volume fractions.

1 Introduction

Polymer matrix composites have become indispensable in advanced engineering applications, such as aerospace, automotive, and high-performance sports equipment, due to their exceptional strength-to-weight ratio [1]. The mechanical behavior of these composites is highly dependent on the type and scale of reinforcement, each offering distinct advantages and presenting specific limitations. CFs, as macroscopic reinforcements, provide the composite with high stiffness, excellent tensile strength, and substantial load-bearing capacity. Their directional nature allows mechanical properties to be tailored along the fiber orientation [2]. However, the inclusion of CFs can increase the overall weight of the composite, and their ability to inhibit microcrack propagation is limited [3]. In contrast, single-walled boron nitride nanotubes (SWBNNTs), acting as nanoscale reinforcements, markedly enhance fracture resistance and durability while adding minimal weight [4]. They also contribute additional functional properties, such as improved thermal and electrical performance. Nevertheless, their widespread application is hindered by challenges related to uniform dispersion within the polymer matrix and relatively high cost. Liu et al. [5] investigated hybrid graphene and carbon nanotube (CNT) reinforced composites with polymer, metal, and ceramic matrices, focusing on their fabrication methods and the resulting mechanical, electrical, and thermal properties. Ahmadi et al. [6] investigated the bending, buckling, and free vibration of hybrid composites with a polymer matrix reinforced with CF/CNT using FEM, Ebrahimi and Dabbagh [7] analyzed the vibrational response of multiscale hybrid nanocomposite plates employing the Halpin Tsai model. Their results showed that these hybrid configurations exhibit superior performance compared to their conventionally reinforced composite counterparts. To combine the advantages of macro- and nanoscale reinforcements while minimizing their individual limitations, hybrid composites integrating both carbon fibers and boron nitride nanotubes have been developed. These materials exhibit enhanced mechanical performance across multiple scales, improved durability, and reduced weight, making them particularly suitable for applications requiring high strength, long-term reliability, and lightweight structures. In this study, the first-order shear deformation shell theory (FSDT) [8] along with the finite element method (FEM) is employed to investigate the static bending behavior of cylindrical shells. To assess the static response of these shells under various boundary conditions, an in-house MATLAB FEM code has been developed, and the results are validated against data available in the literature. Parametric studies are conducted to examine the influence of BNNT and CF volume fractions as well as BNNT distribution patterns on the bending behavior of the reinforced cylindrical shells.

2 Mathematical formulation

2.1 Problem description

As illustrated in Fig. 1, the investigated structure is a composite cylindrical panel composed of a polymer matrix reinforced by a combination of nano- and macro-scale reinforcements. The investigated cylindrical shell panel possesses a length $\boldsymbol{L}$, a radius of curvature $\boldsymbol{R}$, an opening angle $\boldsymbol{\theta_0}$, and a uniform total thickness $\boldsymbol{h}$. The deformation and geometry of the cylindrical shell are represented using a Cartesian coordinate system $(\boldsymbol{O}; \boldsymbol{x}, \boldsymbol{\theta}, \boldsymbol{z})$, where $\boldsymbol{x}, \boldsymbol{\theta}$, and $\boldsymbol{z}$ indicate the longitudinal, tangential, and radial coordinates along the mid-surface of the shell $\boldsymbol{\Omega}$. Different SLs and BCs are imposed on the examined CCPs. The studied composite shell is constituted of a PM simultaneously reinforced with macroscopic and nanoscopic reinforcements, notably SWBNNT nanofillers and macroscopic CF reinforcements, as illustrated in Fig. 1. The distribution of SWBNNTs is assumed to follow an FG-SWBNNT scheme, such as (FG-V-SWBNNT), (FG-O-SWBNNT), and (FG-X-SWBNNT), alongside a uniform distribution (UD-SWBNNT) throughout the thickness of the composite shell. CFs are considered to be uniformly dispersed within the PM.

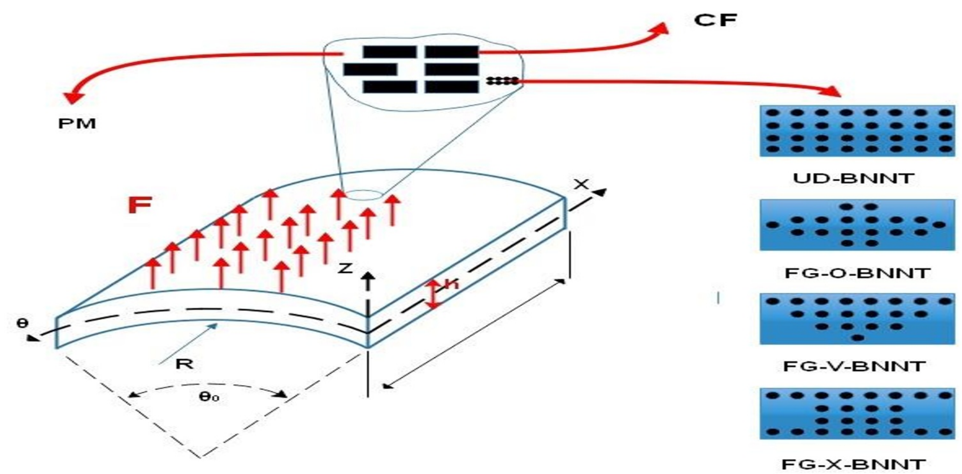

Fig. 1. Geometry of PM/FG-BNNT/CF nanocomposite cylindrical shell subjected to external static mechanical loading with different reinforcement patterns.

2.2 Effective material properties of the PM/BNNT/CF.

The homogenization procedure used is developed through a two-step process, integrating a modified Halpin-Tsai model [9], with a fiber micromechanical approach [10].

2.2.1 Modified Halpin-Tsai model for predicting BNNT/PM material properties

The effective material properties of multiscale nanocomposites, derived using the Halpin–Tsai relation, can be expressed as follows [11]:

$$E_{BNNT/PM}(z) = \alpha_L E_L(z) + \alpha_T E_T(z) \tag{1}$$

here, $\alpha_L = 3/8$ and $\alpha_T = 1 - \alpha_L$, $E_L(z)$ and $E_T(z)$ are calculated as follows:

$$E_L(z) = \frac{1 + \xi_L \eta_L V_{BNNT}(z)}{1 - \eta_L V_{BNNT}(z)} E_{PM} \; ; \; E_T(z) = \frac{1 + \xi_T \eta_T V_{BNNT}(z)}{1 - \eta_T V_{BNNT}(z)} E_{PM} \tag{2}$$

η_L and η_T are given by:

$$\eta_L = \frac{(E_{BNNT}/E_{PM}) - 1}{(E_{BNNT}/E_{PM}) + \xi_L} \; ; \; \eta_T = \frac{(E_{BNNT}/E_{PM}) - 1}{(E_{BNNT}/E_{PM}) + \xi_T} \tag{3}$$

in wich E_{PM}, and E_{BNNT} represent the Young's moduli of the PM material and BNNT nanofillers, respectively The geometric parameters ξ_L and ξ_T are determined as follows:

$$\xi_L = 2\beta_L \; ; \; \xi_T = 2 \tag{4}$$

where β_L denotes the filler aspect ratio, defined as $\beta_L = \frac{L_{BNNT}}{d_{BNNT}} = 300$, with L_{BNNT} and d_{BNNT} representing the length and diameter of the BNNT fillers, respectively. The volume fraction $V_{BNNT}(z)$ for the four FG distribution patterns is determined as follow [12]:

$$V_{BNNT}(z) = \begin{cases} V^*_{BNNT} & \textit{for} \quad \textit{(UD-BNT)} \\ \left(1 + \frac{2z}{h}\right) V^*_{BNNT} & \textit{for} \quad \textit{(FG-V-BNT)} \\ 2\left(1 - \frac{2|z|}{h}\right) V^*_{BNNT} & \textit{for} \quad \textit{(FG-O-BNT)} \\ 2\left(\frac{2|z|}{h}\right) V^*_{BNNT} & \textit{for} \quad \textit{(FG-X-BNT)} \end{cases} \tag{5}$$

Where V^*_{BNNT} denotes the total volume fraction of BNNT, which can be approximated as:

$$V_{BNNT} = \frac{w_{BNNT}}{w_{BNNT} + (\rho_{BNNT}/\rho_m) - (\rho_{BNNT}/\rho_m) w_{BNNT}} \tag{6}$$

The effective Poisson's ratio $v_{BNNT/PM}(z)$ is calculated using the ROM as follows:

$$v_{BNNT/PM}(z) = v_{BNNT} V_{BNNT}(z) + v_{PM} V_{PM}(z) \tag{7}$$

where $V_{BNNT}(z)$ and $V_{PM}(z)$ denote the volume fractions of the BNNT and PM reinforcement, respectively. The volume fraction of the PM is provided by the following relation:

$$V_{PM}(z) = 1 - V_{BNNT}(z) \tag{8}$$

The effective shear modulus $G_{BNNT/PM}$ can be calculated as follows:

$$G_{BNNT/PM}(z) = \frac{E_{BNNT/PM}(z)}{2\left(1 + v_{BNNT/PM}(z)\right)} \tag{9}$$

2.2.2 Micromechanical scheme for predicting the material properties of BNNT/CF reinforced PM

The effective mechanical properties of the FG-BNNT/CF-reinforced PM are determined using the micromechanical approach as follows [13]:

$$\left\{\begin{array}{c} E_{11}^{eff}(z) = V_{cf}(z)E_{11}^{cf} + V_{BNNT/PM}E^{BNNT/PM} \\ \dfrac{1}{E_{22}^{eff}(z)} = \dfrac{1}{E_{22}^{CF}} + \dfrac{V_{BNNT/PM}}{E^{BNNT/PM}} - V_{cf}V_{BNNT/PM} \\ -\dfrac{v_{CF}^2\dfrac{E^{BNNT/PM}}{E_{22}^{CF}} + v_{BNNT/PM}^2\dfrac{E_{22}^{CF}}{E^{BNNT/PM}} - 2v_{CF}v_{BNNT/PM}}{v_{CF}E_{22}^{CF} + v_{BNNT/PM}E^{BNNT/PM}} \\ \dfrac{1}{G_{12}^{eff}(z)} = \dfrac{V_{CF}}{G_{12}^{CF}} + \dfrac{V_{BNNT/PM}}{G^{BNNT/PM}} \\ v_{12}^{eff}(z) = V_{CF}v_{CF} + V_{BNNT/PM}v_{BNNT/PM} \end{array}\right. \quad (10)$$

Where E, G, v denote the Young's modulus, shear modulus and Poisson's ratio, respectively. In Eq. (11), the superscripts CF and BNNT/PM refer to carbon fiber and BNNT reinforced PM, respectively. Additionally, V_{CF} and $V_{BNNT/PM}$ represent the volume fractions of carbon fiber and the polymer matrix reinforced with BNNT, respectively, and they are related as follows:

$$V_{CF} + V_{BNNT/PM} = 1 \quad (11)$$

The material properties of the PM, BNNT, and CF are listed in Table 1.

Table 1. Material properties of the PM, BNNT, and PM.

Parameter	Values
E_{PM}(GPa)	2.5
v_{PM}	0.3
ρ_{PM}(kg/m^3)	1190
E_{BNNT}(TPa)	1.064
v_{BNNT}	0.14
ρ_{BNNT}(kg/m^3)	2270
E_{CF}(GPa)	233.05
G_{CF}(GPa)	8.96
v_{CF}	0.2
ρ_{CF}(kg/m^3)	1750

2.3 Displacement field

The displacement field of the FSDT is of the form:

$$\begin{aligned} U_x(x,\theta,z,t) &= u_x(x,\theta) + z\phi_x(x,\theta) \\ U_\theta(x,\theta,z,t) &= u_\theta(x,\theta) + z\phi_y(x,\theta) \\ U_z(x,\theta,z,t) &= u_z(x,\theta) \end{aligned} \tag{12}$$

where $\boldsymbol{u_x}$, $\boldsymbol{u_\theta}$ and $\boldsymbol{u_z}$ are the displacement components in $\boldsymbol{x}$, $\boldsymbol{\theta}$, and $\boldsymbol{z}$ directions, respectively.

2.4 Strain field

The strain components are given by:

$$\begin{cases} \epsilon_{xx} &= \dfrac{\partial u_x}{\partial x} + z\dfrac{\partial \phi_x}{\partial x} \\ \epsilon_{\theta\theta} &= \dfrac{1}{R}\dfrac{\partial u_\theta}{\partial \theta} + \dfrac{u_z}{R} + \dfrac{z}{R}\dfrac{\partial \phi_\theta}{\partial \theta} \\ \gamma_{x\theta} &= \dfrac{1}{R}\dfrac{\partial u_x}{\partial \theta} + \dfrac{\partial u_\theta}{\partial x} + z\left(\dfrac{1}{R}\dfrac{\partial \phi_x}{\partial\, \theta} + \dfrac{\partial \phi_\theta}{\partial x}\right) \\ \gamma_{xz} &= \phi_x + \dfrac{\partial u_z}{\partial x} \\ \gamma_{\theta z} &= \dfrac{1}{R}\dfrac{\partial u_z}{\partial \theta} + \phi_\theta - \dfrac{u_\theta}{R} \end{cases} \tag{13}$$

2.5 Constitutive Relations

The constitutive relations are expressed as:

$$\begin{bmatrix} \sigma_{xx} \\ \sigma_{\theta\theta} \\ \tau_{x\theta} \end{bmatrix} = \begin{bmatrix} Q_{11} & Q_{12} & 0 \\ Q_{12} & Q_{22} & 0 \\ 0 & 0 & Q_{66} \end{bmatrix} \begin{bmatrix} \epsilon_{xx} \\ \epsilon_{\theta\theta} \\ \gamma_{x\theta} \end{bmatrix} \tag{14}$$

$$\begin{bmatrix} \tau_{Xz} \\ \tau_{\theta z} \end{bmatrix} = \begin{bmatrix} Q_{44} & 0 \\ 0 & Q_{55} \end{bmatrix} \begin{bmatrix} \gamma_{xz} \\ \gamma_{\theta z} \end{bmatrix} \tag{15}$$

where the parameters $Q_{11}, Q_{22}, Q_{12}, Q_{44} Q_{55}$ and Q_{66} are given as:

$$\begin{cases} Q_{11} & = & \dfrac{E_{11}^{eff}}{1-(v_{12}^{eff})^2} \\ Q_{22} & = & \dfrac{E_{22}^{eff}}{1-(v_{12}^{eff})^2} \\ Q_{12} & = & \dfrac{v_{12}^{eff}E_{11}^{eff}}{1-(v_{12}^{eff})^2} \\ Q_{66} & = & G_{12}^{eff} \\ Q_{44} & = & G_{12}^{eff} \\ Q_{55} & = & G_{12}^{eff} \end{cases} \tag{16}$$

2.6 Energy functionals

The strain energy of the considered cylindrical shell is expressed by:

$$\pi_\epsilon = \frac{1}{2}\int_0^L \int_0^{\theta_0} \boldsymbol{\epsilon}^T \boldsymbol{R}_{eff} \boldsymbol{\epsilon} R d\theta dx \tag{17}$$

where $\boldsymbol{\epsilon}$ is given by:

$$\boldsymbol{\epsilon} = \begin{bmatrix} \boldsymbol{\epsilon}_m \\ \boldsymbol{\epsilon}_b \\ \boldsymbol{\epsilon}_s \end{bmatrix} \tag{18}$$

in which

$$\boldsymbol{\epsilon}_m = \begin{bmatrix} \dfrac{\partial \mathrm{u_x}}{\partial \mathrm{x}} \\ \dfrac{1}{\mathrm{R}}\dfrac{\partial \mathrm{u_\theta}}{\partial \theta} + \dfrac{\mathrm{u_z}}{\mathrm{R}} \\ \dfrac{1}{\mathrm{R}}\dfrac{\partial \mathrm{u_x}}{\partial \theta} + \dfrac{\partial \mathrm{u_\theta}}{\partial \mathrm{x}} \end{bmatrix}; \boldsymbol{\epsilon}_b = \begin{bmatrix} \dfrac{\partial u_x}{\partial x} \\ \dfrac{1}{R}\dfrac{\partial \phi_\theta}{\partial \theta} \\ \dfrac{1}{R}\dfrac{\partial \phi_x}{\partial \theta} + \dfrac{\partial \phi_\theta}{\partial x} \end{bmatrix}; \boldsymbol{\epsilon}_s = \begin{bmatrix} \dfrac{\partial v_z}{\partial x} + \phi_x \\ \dfrac{1}{R}\dfrac{\partial u_z}{\partial \theta} + \phi_y - \dfrac{u_\theta}{R} \end{bmatrix} \tag{19}$$

$$\boldsymbol{R}_{eff} = \begin{bmatrix} R_{11}^m & R_{12}^m & R_{16}^m & R_{11}^{mb} & R_{12}^{mb} & R_{16}^{mb} & 0 & 0 \\ R_{12}^m & R_{22}^m & R_{26}^m & R_{12}^{mb} & R_{22}^{mb} & R_{26}^{mb} & 0 & 0 \\ R_{16}^m & R_{26}^m & R_{66}^m & R_{16}^{mb} & R_{26}^{mb} & R_{66}^{mb} & 0 & 0 \\ R_{11}^{mb} & R_{12}^{mb} & R_{16}^{mb} & R_{11}^b & R_{12}^b & R_{16}^b & 0 & 0 \\ R_{12}^{mb} & R_{22}^{mb} & R_{26}^{mb} & R_{12}^b & R_{22}^b & R_{26}^b & 0 & 0 \\ R_{16}^{mb} & R_{26}^{mb} & R_{66}^{mb} & R_{16}^b & R_{26}^b & R_{66}^b & 0 & 0 \\ 0 & 0 & 0 & 0 & 0 & 0 & R_{44}^s & R_{45}^s \\ 0 & 0 & 0 & 0 & 0 & 0 & R_{45}^s & R_{55}^s \end{bmatrix} \tag{20}$$

Where the extensional R_{ij}^{m}, coupling R_{ij}^{mb}, bending R_{ij}^{b}, and thansverse shear R_{ij}^{s} stiffnesses are defined as:

$$\left(R_{ij}^{m}, R_{ij}^{mb}, R_{ij}^{b}, R_{ij}^{s}\right) = \int_{-\frac{h}{2}}^{+\frac{h}{2}} Q_{ij}(1, z, z^2, k_s)dz \tag{21}$$

Where k_s is the shear correction factor taken in this work equal to $5/6$. The external work energy due to the external forces is given by

$$w_e = \int_0^L \int_0^{\theta_0} \boldsymbol{u}^\top \boldsymbol{f} R d\theta dx \tag{22}$$

where $\boldsymbol{f}$ is the external load vector.

The total potential energy of the shell panel is expressed as.

$$\Pi = \pi_\epsilon - w_e \tag{23}$$

3 Finite Element Methodology

In this work the finite element method is used to find the deflection of the cylindrical shell panel under static mechanical loads. The field variables are expressed in terms of shape function using interpolation as:

$$\boldsymbol{q} = \sum_{i=1}^{4} \boldsymbol{I_4} \boldsymbol{N}_i \boldsymbol{q}_i \tag{24}$$

where $\boldsymbol{q}_i$ denotes the vector of the five nodal field variables at the i^{th}node, given as:

$$\boldsymbol{q_i} = \left[\boldsymbol{u_x^i}, \boldsymbol{u_\theta^i}, \boldsymbol{u_z^i}, \boldsymbol{\phi_x^i}, \boldsymbol{\phi_\theta^i}\right]^\top \tag{25}$$

and, $\boldsymbol{N}_i$ is the corresponding shape function expressed as:

$$\begin{aligned} N_1 &= \frac{1}{4}(1-\xi)(1-n) \\ N_2 &= \frac{1}{4}(1+\xi)(1-\eta) \\ N_3 &= \frac{1}{4}(1+\xi)(1+\eta) \\ N_4 &= \frac{1}{4}(1-\xi)(1+\eta) \end{aligned} \tag{26}$$

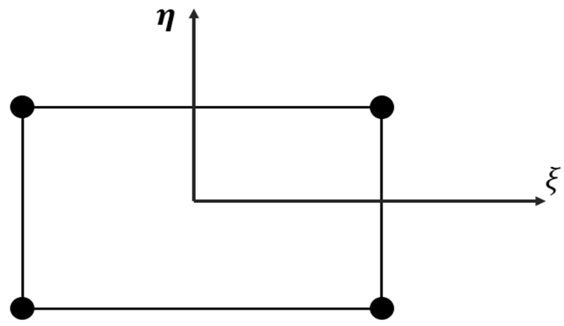

Fig. 2. Quadrilateral Q4 element in natural coordinates

and $\boldsymbol{I}_5$ is the identity matrix of order four. After applying the FE method we obtain:

$$\boldsymbol{K}\boldsymbol{q} = \boldsymbol{F} \tag{27}$$

Where $\boldsymbol{K}$ and $\boldsymbol{F}$ are the global stifness matrix and global load vector.

$$\begin{aligned} \boldsymbol{K} &= \int_0^L \int_0^{\theta_0} \boldsymbol{B}^T \boldsymbol{R}_{eff} \boldsymbol{B} R d\theta dx \\ \boldsymbol{F} &= \int_0^L \int_0^{\theta_0} \boldsymbol{\Psi}^T \boldsymbol{f}\, R d\theta dx \end{aligned} \tag{28}$$

Where the differential strain matrix $\boldsymbol{B}$ is given by:

$$\boldsymbol{B} = \begin{bmatrix} \boldsymbol{B}^m \\ \boldsymbol{B}^b \\ \boldsymbol{B}^s \end{bmatrix} \tag{29}$$

$$\boldsymbol{B}^m = \sum_{i=1}^{4} \begin{bmatrix} \frac{\partial N_i}{\partial x} & 0 & 0 & 0 & 0 \\ 0 & \frac{1}{R}\frac{\partial N_i}{\partial \theta} & \frac{N_i}{R} & 0 & 0 \\ \frac{1}{R}\frac{\partial N_i}{\partial \theta} & \frac{\partial N_i}{\partial x} & 0 & 0 & 0 \end{bmatrix} \tag{30}$$

$$\boldsymbol{B}^b = \sum_{i=1}^{4} \begin{bmatrix} 0 & 0 & 0 & \frac{\partial N_i}{\partial x} & 0 \\ 0 & 0 & 0 & 0 & \frac{1}{R}\frac{\partial N_i}{\partial \theta} \\ 0 & 0 & 0 & \frac{1}{R}\frac{\partial N_i}{\partial \theta} & \frac{\partial N_i}{\partial x} \end{bmatrix} \tag{31}$$

$$\boldsymbol{B}^s = \sum_{i=1}^{4} \begin{bmatrix} 0 & 0 & \frac{\partial N_i}{\partial x} & N_i & 0 \\ 0 & -\frac{N_i}{R} & \frac{1}{R}\frac{\partial N_i}{\partial \theta} & 0 & N_i \end{bmatrix} \tag{32}$$

$$\boldsymbol{\Psi}^T = \sum_{i=1}^{4} \begin{bmatrix} N_i & 0 & 0 & 0 & 0 \\ 0 & N_i & 0 & 0 & 0 \\ 0 & 0 & N_i & 0 & 0 \\ 0 & 0 & 0 & N_i & 0 \\ 0 & 0 & 0 & 0 & N_i \end{bmatrix} \tag{33}$$

4 Results and discussion

This section focuses on the investigation of the linear static behavior of PM/FG-BNNT/CF nanocomposite cylindrical shells subjected to uniformly distributed transverse mechanical loads under various boundary conditions. The results obtained from the proposed numerical model are compared with those available in the literature. In addition, parametric studies are carried out to examine the influence of different parameters on the mechanical response of the PM/FG-BNNT/CF nanocomposite cylindrical shells

4.1 Convergence study

To evaluate the accuracy and validity of the current numerical model using FEM based on FSDT, convergence studies were first performed on a fully clamped (CCCC) elastic homogeneous isotropic cylindrical shell subjected to a uniformly distributed load (UDL) of magnitude $p_0 = 0.04psi$. The geometric dimensions of the panel are [14]: $L = 20\text{in}, R = 100\text{in}, h = 0.125\text{in}$, and $\theta_0 = 0.2\text{rad}$. The material properties of the panel are: $E = 0.45 \times 10^6 psi$ and $v = 0.3$. Various numbers of elements $6 \times 6, 8 \times 8, 10 \times 10, 12 \times 12, 16 \times 16, 20 \times 20, 26 \times 26$, and 30×30 are examined. Table 2 illustrates a comparison between the vertical displacements at the shell panel center obtained using the proposed numerical model and those reported by Reddy [14].

Table 2. Central deflection u_z (in) with different numbers of elements N_{elem} of a CCCC cylindrical shell panel under UDL

N_{elem}	Present	Reddy [15]
6 × 6	0.01292	0.01134
8 × 8	0.01214	
10 × 10	0.01181	
12 × 12	0.01164	
16 × 16	0.01148	
20 × 20	0.01141	
26 × 26	0.01136	
30 × 30	0.01134	

The results presented in Table 2 demonstrate that the predictions obtained with the proposed numerical method are in excellent agreement with those reported by Reddy [15]. Based on a balance between accuracy and computational efficiency, a 30×30 elements is adopted for all subsequent simulations.

4.2 Validation

This numerical study focuses on square FG cylindrical shell composed of $\mathrm{Al/ZrO_2}$ subjected to UDL of intesity $p_0 = 1 \times 10^6\ \mathrm{N/m^2}$ with CCCC and SSSS ECs. Different values of volume fractions $n \in [0,0.2,0.5,1,2,5]$ are considered in the comparison. The shell's geometric characteristics are outlined as follows [15]: $L = 0.2$ m, $R = 1$ m, $h = 0.01$ m, and $\theta_0 = 0.2\mathrm{rad}$. The material properties of the analyzed FG shells are [15]: $E_{Al} = 70 \times 10^9\ \mathrm{N/m^2}$, $E_{\mathrm{ZrO_2}} = 151 \times 10^9\ \mathrm{N/m^2}$, $v_{Al} = v_{\mathrm{ZrO_2}} = 0.3$. Table 3 reports the nondimensional central deflections of Al/ZrO_2 shells corresponding to different volume fraction values.

Table 3. Central deflection u_z of a CCCC FG cylindrical shell panel under UDL

n	SSSS		CCCC	
	Present	**Zhao et al [16]**	**Present**	**Zhao et al [16]**
0	0.0422	0.0426	0.0136	0.0134
0.2	0.0475	0.0480	0.0153	0.0151
0.5	0.0537	0.0543	0.0173	0.0171
1	0.0601	0.0607	0.0194	0.0191
2	0.0659	0.0665	0.0213	0.0210
5	0.0716	0.0723	0.0231	0.0228

The results shown in Table 3 reveal a strong agreement between the present findings and those available in the literature by Zhao et al. [16]. Furthermore, the results indicate that increasing the power-law index (n) reduces the stiffness of the FG shell, which in turn leads to larger deflections.

4.3 Parametric analysis

In this subsection, we present results to investigate the impact of various geometric and material parameters on the linear static response of PM/FG-BNNT/CF nanocomposite cylindrical shells. The cylindrical shell considered in this study has an opening angle of $\theta_0 = 0.1\mathrm{rad}$, a thickness of $h = 0.002$ m, a radius of $R = 1$ m, and a length of $a = 0.1$ m, and it is subjected to a uniformly distributed transverse load of magnitude $p_0 = 0.1 \times 10^6\ \mathrm{N/m^2}$.

4.3.1 Influence of BNNT distribution patterns

In order to study the influence of the type of SWBNNT distribution on the central vertical displacement of the shell. We consider respectively four distributions of SWBNNT, which are: UD ,FG-V,FG-O,FG-X with a weight fraction value (SWCNT) of 0.01.

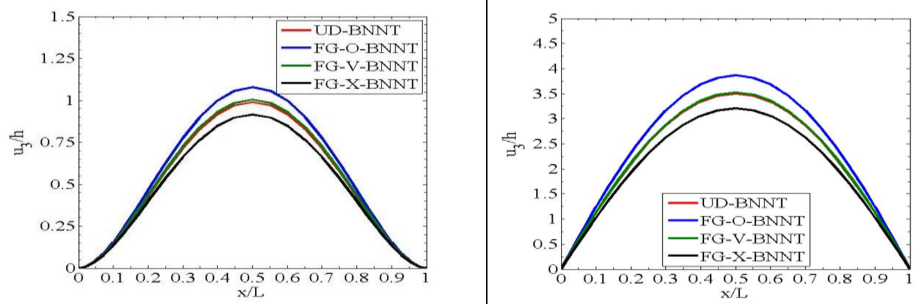

1(a) 2(b)

Fig. 3. Nondimensional vertical displacement u_z/h along the centreline (x, $\theta_0/2$) versus x/L for different BNNT distribution patterns of FG-BNNT-CF reinforced cylindrical panel under DL with CCCC (3(a)) and SSSS(3(b)) BCs

From Fig.3 we notice that the maximum value of the central transverse displacement corresponds to the FG-O distribution and that the minimum value corresponds to the FG-X. For the FG-V and UD the deformation is higher than the FG-O and smaller than the FG-X. Therefore, it can be concluded that placing BNNTs near the top and bottom surfaces of PM/FG-BNNT/CF nanocomposite cylindrical shells is the optimal strategy to enhance the overall rigidity of the shells, as this placement maximizes the moment of inertia and improves the shells' resistance to bending under static loads.

4.3.2 Influence of BNNT weight fraction

To assess the impact of BNNT volume fraction V_{BNNT} on the vertical displacement of PM/FG-BNNT/CF nanocomposite cylindrical shells, we consider CCCC and SSSS BCs with a UD load. The CF volume fraction is set at 0 with an FG-X distribution pattern. Figs. 4(a) and 4(b) display the nondimensional central vertical displacement of FG-BNNT-CF reinforced CCPs with different values of BNNT weight fractions.

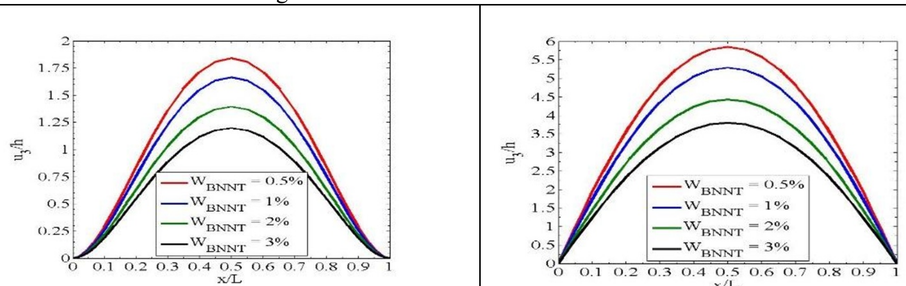

(a) (b)

Fig. 4. Nondimensional vertical displacement u_z/h along the centreline (x, $\theta_0/2$) versus x/L for FG-BNNT-CF reinforced cylindrical panel, CF with varying BNNT weight fractions under UDL with CCCC (4(a)) and SSSS (4(b)) boundary conditions

Figures 4(a) and 4(b) show that increasing the BNNT weight fraction $\boldsymbol{W_{\mathrm{BNNT}}}$ influences the central vertical displacement of PM/FG-BNNT/CF nanocomposite cylindrical shells. Specifically, higher BNNT weight fractions lead to a reduction in the central displacement, because increased reinforcement content enhances the stiffness and mass distribution of the shell, with this effect being significant under all considered boundary conditions. Moreover, the minum central displacement is observed under CCCC boundary conditions, while the SSSS shells consistently exhibit higher displacements compared to SSSS cases.

4.3.3 Influence of CF volume fraction

In the last examination, the impact of CF volume fraction VCF on the central vertical displacement of the shell with FG-O distributions is investigated. The Fig. 5 show the central transverse displacement for C-F and C-C FG- of PM/FG-BNNT/CF nanocomposite cylindrical shells with the value of volume fraction 0.03, 0.05 and 0.1.

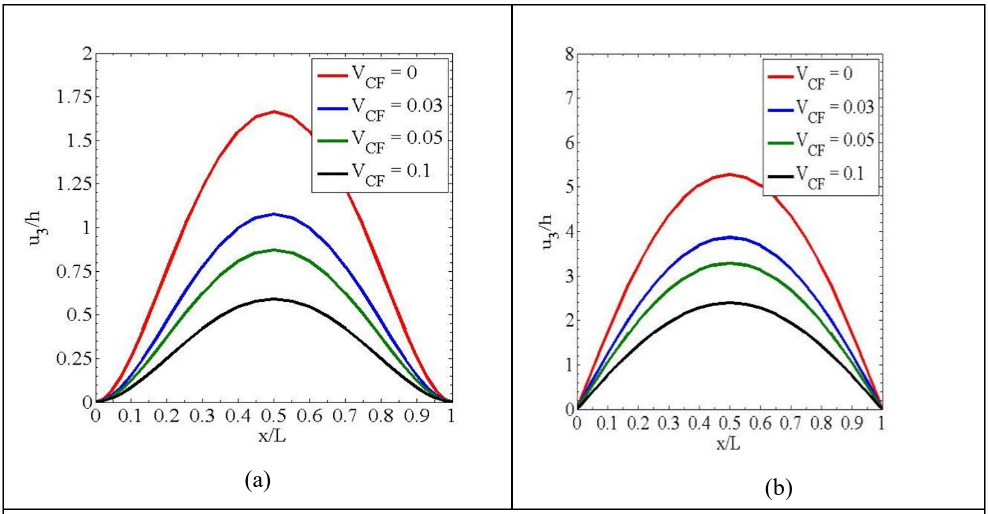

Fig.5. Nondimensional vertical displacement u_z/h along the centreline (x, $\theta_0/2$) versus x/L for FG-BNNT-CF reinforced cylindrical panel, with varying CF weight fractions under UDL with CCCC (5(a)) and SSSS(5(b)) BCs

It can be seen From Fig. 5, that the decrease of the CF volume fraction leads to an increase of central vertical displacement of the shell, due to the superior load-bearing performance of the CF. Moreover, the minimum central displacement is observed under CCCC BCs, while the SSSS shells consistently exhibit higher displacements compared to both CCCC.

5 Conclusion

This paper has presented a detailed bending analysis of polymer matrix (PM) cylindrical shells reinforced with functionally graded boron nitride nanotubes (FG-BNNTs) and carbon fibers (CFs), employing the finite element (FE) method based on the FSDT. The developed model effectively captures the influence of material gradation, reinforcement distribution, and boundary conditions on the static response of nanocomposite cylindrical shells. The numerical results demonstrate the significant role of FG-BNNTs and CFs in enhancing the stiffness and load-carrying capacity of the structure, while the FSDT-based FE formulation provides accurate predictions of the displacement and stress fields. The findings offer valuable insights into the mechanical behavior of advanced nanocomposite cylindrical shells, which can serve as a foundation for the design and optimization of high-performance lightweight structures in engineering applications.

References

[1] D. Gay, *Composite Materials: Design and Applications*, 4th ed. Boca Raton: CRC Press, 2022. doi: 10.1201/9781003195788.

[2] M. R. Zakaria, H. Md Akil, M. H. Abdul Kudus, F. Ullah, F. Javed, and N. Nosbi, “Hybrid carbon fiber-carbon nanotubes reinforced polymer composites: A review,” *Compos. Part B Eng.*, vol. 176, p. 107313, Nov. 2019, doi: 10.1016/j.compositesb.2019.107313.

[3] N. Hiremath, J. Mays, and G. Bhat, “Recent Developments in Carbon Fibers and Carbon Nanotube-Based Fibers: A Review,” *Polym. Rev.*, vol. 57, no. 2, pp. 339–368, Apr. 2017, doi: 10.1080/15583724.2016.1169546.

[4] C. Zhi, Y. Bando, C. Tang, and D. Golberg, “Boron nitride nanotubes,” *Mater. Sci. Eng. R Rep.*, vol. 70, no. 3–6, pp. 92–111, Nov. 2010, doi: 10.1016/j.mser.2010.06.004.

[5] B. Liu, J. Sun, J. Zhao, and X. Yun, Hybrid graphene and carbon nanotube–reinforced composites: polymer, metal, and ceramic matrices, Adv. Compos. Hybrid Mater., vol. 8, no. 1, pp. 1–24, 2025. doi: 10.1007/s42114-024-01074-3.

[6] M. Ahmadi, R. Ansari, and H. Rouhi, "Studying buckling of composite rods made of hybrid carbon fiber/carbon nanotube-reinforced polyimide using multi-scale FEM," *Scientia Iranica*, vol. 27, no. 1, pp. 252–261, 2020. doi: 10.24200/sci.2018.5722.1444

[7] F. Ebrahimi et A. Dabbagh, "Vibration analysis of multi-scale hybrid nanocomposite plates based on a Halpin-Tsai homogenization model," *Compos. Part B Eng.*, vol. 173, p. 106955, 2019

[8] Z. X. Lei, L. W. Zhang, and K. M. Liew, “Elastodynamic analysis of carbon nanotube-reinforced functionally graded plates,” *Int. J. Mech. Sci.*, vol. 99, pp. 208–217, Aug. 2015, doi: 10.1016/j.ijmecsci.2015.05.014.

[9] M. Fouaidi, M. Jamal, A. Zaite, and N. Belouaggadia, “Bending analysis of functionally graded graphene oxide powder-reinforced composite beams using a meshfree method,” *Aerosp. Sci. Technol.*, vol. 110, p. 106479, Mar. 2021, doi: 10.1016/j.ast.2020.106479.

[10] E. T. Thostenson, W. Z. Li, D. Z. Wang, Z. F. Ren, and T. W. Chou, “Carbon nanotube/carbon fiber hybrid multiscale composites,” *J. Appl. Phys.*, vol. 91, no. 9, pp. 6034–6037, May 2002, doi: 10.1063/1.1466880.

[11] A. A. Yazdi, “Nonlinear aeroelastic stability analysis of three-phase nano-composite plates,” *Mech. Based Des. Struct. Mach.*, vol. 47, no. 6, pp. 753–768, Nov. 2019, doi: 10.1080/15397734.2019.1610436.

[12] E. Sobhani and M. Avcar, “The influence of various nanofiller materials (CNTs, GNPs, and GOPs) on the natural frequencies of Nanocomposite Cylindrical Shells: A comparative study,” *Mater. Today Commun.*, vol. 33, p. 104547, Dec. 2022, doi: 10.1016/j.mtcomm.2022.104547.

[13] A. A. Yazdi, “Nonlinear aeroelastic stabilit y analysis of three-phase nano-composite plates,” *Mech. Based Des. Struct. Mach.*, vol. 47, no. 6, pp. 753–768, Nov. 2019, doi: 10.1080/15397734.2019.1610436.

[14] J. N. Reddy, Mechanics of Laminated Composite Plates and Shells: Theory and Analysis, CRC Press, 2003.

[15] X. Zhao, Y. Lee, and K. M. Liew, “Thermoelastic and vibration analysis of functionally graded cylindrical shells,” Int. J. Mech. Sci., vol. 51, no. 9–10, pp. 694–707, 2009, doi: 10.1016/j.ijmecsci.2009.08.001.